Research Article Vol. 13, No. 3 / 1 Mar 2023 / Optical Materials Express 752

Optical Materials EXPRESS

Sharp MIR plasmonic modes in gratings made of heavily doped pulsed laser-melted $Ge_{1-x}Sn_x$

F. Berkmann,[1,*] O. Steuer,[2] F. Ganss,[2] S. Prucnal,[2] D. Schwarz,[1] I. A. Fischer,[3] and J. Schulze[4]

[1] *Institute of Semiconductor Engineering, University of Stuttgart, 70569 Stuttgart, Germany*
[2] *Institute of Ion Beam Physics and Materials Research, Helmholtz-Zentrum Dresden-Rossendorf, 01328 Dresden, Germany*
[3] *Institute of Experimental Physics and Functional Materials, Brandenburg University of Technology, 03046 Cottbus, Germany*
[4] *Chair of Electron Devices (LEB), FAU Erlangen-Nuremberg, 91054 Erlangen, Germany*
[*] *Fritzberkmann@gmail.com*

Abstract: Plasmonic structures made out of highly doped group-IV semiconductor materials are of large interest for the realization of fully integrated mid-infrared (MIR) devices. Utilizing highly doped $Ge_{1-x}Sn_x$ alloys grown on Si substrates is one promising route to enable device operation at near-infrared (NIR) wavelengths. Due to the lower effective mass of electrons in Sn compared to Ge, the incorporation of Sn can potentially lower the plasma wavelength of $Ge_{1-x}Sn_x$ alloys compared to that of pure Ge. However, defects introduced by the large lattice mismatch to Si substrates as well as the introduction of alloy scattering limit device applications in practice. Here, we investigate pulsed laser melting as one strategy to increase material quality in highly doped $Ge_{1-x}Sn_x$ alloys. We show that a pulsed laser melting treatment of our $Ge_{1-x}Sn_x$ films not only serves to lower the material's plasma frequency but also leads to an increase in active dopant concentration. We demonstrate the application of this material in plasmonic gratings with sharp optical extinction peaks at MIR wavelengths.

Published by Optica Publishing Group under the terms of the Creative Commons Attribution 4.0 License. Further distribution of this work must maintain attribution to the author(s) and the published article's title, journal citation, and DOI.

1. Introduction

Plasmonic structures such as plasmonic antennas are of large interest for the manipulation of light-matter interaction, which can be used for applications in sensing [1,2] and for enabling [3,4] or enhancing [5] optoelectronic device functionality. Highly doped semiconductors are promising materials for expanding the wavelength range of plasmonic applications towards mid infrared (MIR) wavelengths [6–8]. In contrast to metals such as gold or silver, which are often used for plasmonic applications at wavelengths in the visible region, the lower carrier density of highly doped semiconductors such as Ge_xSn_{1-x} can lead to lower damping at MIR wavelengths. In addition, $Ge_{1-x}Sn_x$ based plasmonic structures are potentially CMOS-compatible, enabling easy and scalable as well as cost-effective fabrication. Using pulsed laser melting (PLM), high carrier concentrations of 2.6 $10^{20}\,cm^{-3}$ and a plasma wavelength of $\lambda_p = 2.6\,\mu m$ were achieved in n-Ge films [9] and antennas made from heavily n-type doped Ge were used to enhance the signal in Fourier-transform infrared spectroscopy (FTIR)-based sensing [10].

The permittivities of highly n-doped Ge and Ge_xSn_{1-x} alloys at large wavelengths are well described by a Drude model [11,12]. The materials can support plasmonic excitations at frequencies below the plasma frequency $\omega_p = \sqrt{\frac{N_{D,ex}e^2}{m_c\varepsilon_\infty\varepsilon_0}}$, where $N_{D,\,ex}$ is the dopant concentration, m_c is the electron effective mass, e is the electron charge, ε_∞ is the high-frequency dielectric screening constant and ε_0 is the free space permittivity. Since the effective mass of Sn is lower than the effective mass of Ge, the incorporation of Sn into the Ge matrix leads to a lower effective

#479637 https://doi.org/10.1364/OME.479637
Journal © 2023 Received 31 Oct 2022; revised 19 Jan 2023; accepted 9 Feb 2023; published 24 Feb 2023

mass of the resulting alloy semiconductor compared to pure Ge [13]. This can potentially be used to further increase (lower) the plasma frequency (wavelength) of such materials [8], putting it even closer to the near infrared (NIR) and allowing plasmonic devices to operate at even shorter wavelengths [12]. The characterization of $Ge_{1-x}Sn_x$ films directly grown on Si substrates, however, showed that the degradation in crystal quality due to the larger lattice mismatch between film and substrate actually limits the performance of these layers in plasmonic applications: the lattice constant of Sn ($a_{0,Sn} = 6.489$ Å) is markedly larger than that of Ge ($a_{0,Ge} = 5.658$ Å), which makes the growth of high-quality $Ge_{1-x}Sn_x$ alloys on Si substrates challenging and results in lower relaxation times in the highly doped alloys as compared to Ge [11]. This decrease in relaxation times leads to a broadening of the plasmonic resonances of e.g. plasmonic grating antennas, limiting their usefulness for applications. Improving material quality, therefore, is of vital importance in order to demonstrate the practical benefits of introducing Sn into the Ge matrix.

Here, we investigate two strategies to this end: While still deposited onto Si wafers, our highly n-type doped $Ge_{1-x}Sn_x$ films are grown on top of a $Ge_{1-x}Sn_x$ buffer layer deposited onto a Ge virtual substrate in order to reduce defects arising from the large lattice mismatch of the alloy to the Si substrate. To further increase crystal quality as well as the active doping concentration the films were treated via PLM after deposition. We report on characterization results obtained via FTIR measurements for the unstructured films as well as comb-like grating antennas. Comparing different Sn concentrations as well as different energy densities of the PLM process, we show that the incorporation of Sn can improve the plasmonic behaviour of $Ge_{1-x}Sn_x$ compared to Ge in our samples, highlighting the potential of the group IV alloy for plasmonic applications.

2. Methods and fabrication

Four different samples with varying Sn concentrations were grown via molecular beam epitaxy (MBE) on 4-inch Si (100) substrates with a sheet resistance of 10 Ωcm ≤ ρ ≤ 20 Ωcm. The native oxide was removed via a thermal desorption step at a substrate temperature of T = 900°C for t = 5 min [14]. After the deposition of 50 nm Si at $T_S = 600°C$, to flatten the surface and cover remaining surface contaminants, 100 nm Ge were deposited at $T_S = 330°C$. A t = 5 min long annealing step at T = 830°C was employed to form the virtual substrate (VS). Afterwards, a graded buffer with a thickness of 500 nm for all samples was deposited by introducing a linear, sample-dependent increase of the Sn concentration from $c_{Sn} = 0.1\%$ to the targeted Sn concentration. At the same time, the substrate temperature was decreased linearly from $T_S = 200°C$ to $T_S = 160°C$ to improve the growth towards increasing Sn concentration and to achieve the best possible crystal quality [15]. The growth continued with a 200 nm thick p-type doped $Ge_{1-x}Sn_x$ layer with an acceptor concentration of $N_A = 1\times 10^{17}\,cm^{-3}$, above the expected background doping concentration of $N_A \sim 1 \times 10^{16}\,cm^{-3}$ [16], followed by the final 400 nm thick n-type doped $Ge_{1-x}Sn_x$ layer, with a donor concentration of $N_D = 3 \times 10^{20}\,cm^{-3}$. This pn-junction serves to restrict the current flow between layers during Hall measurements. Both $Ge_{1-x}Sn_x$ layers were grown at $T_S = 160°C$. The doping was realized via in-situ co-evaporation of Sb for the n^{++} layer and B for the p-type layer, respectively. The nominal Sn concentrations were chosen to be $c_{Sn,\,nom}$={0, 2.5, 5.0, 7.5} %. As we will discuss, the actual concentrations c_{Sn}={0, 2.9, 5.3, 6.3} %. obtained from XRD measurements deviate slightly from the nominal ones and will be used in the following to identify the samples.

All samples were diced into 35 × 35 mm^2 pieces prior to pulsed laser melting with two different energy densities and, afterwards, structuring of the plasmonic gratings. The pulsed leaser melting was carried out with a XeCl excimer laser at a wavelength of 308 nm and a pulse length of 28 ns. An area of 5 5 mm^2 in the sample centre was annealed. The energy densities of the laser pulses were set at 0.3 J/cm^2 and 0.5 J/cm^2.

Optical Materials EXPRESS

The plasmonic antennas shaped as comb-like gratings were structured via optical lithography followed by an inductively coupled plasma RIE etching step with an etching depth of 400 nm, equal to the thickness of the topmost n-doped $Ge_{1-x}Sn_x$ layer (Fig. 1 b). The grating structures serve as antennas under illumination with light polarized perpendicularly to the long axis of the gratings. The comb-like geometry ensures that all grating strips can be easily contacted simultaneously e.g., for possible applications in hot-electron photodetection [17]. Afterwards the samples were cleaned using an ultrasonic acetone bath for t = 8 min followed by an ultrasonic bath in isopropanol for t = 2 min. Fig. 1 shows a scanning electron microscope (SEM) image as well as schematic images of the structures and Table 1 lists the geometry parameters of the comb-like antennas. The geometry parameters were chosen based on FDTD simulations, using Drude parameters determined for the PLM-treated layers, with the aim of obtaining well-defined peaks in the extinction spectra in a wavelength range of 12-15 μm.

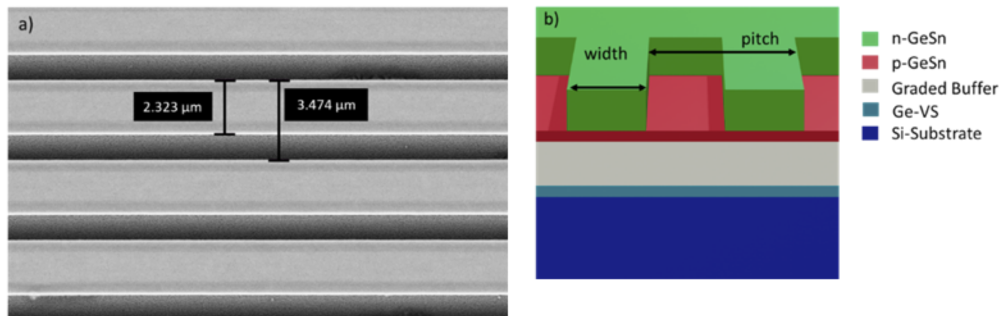

Fig. 1. Top view SEM image (a) and schematic cross section (b) of a comb-like antenna. The graded buffer (grey layer) contains a GeSn alloy with linearly increasing Sn concentration starting at 0.1% of Sn and ending at the targeted Sn content. For the sample without Sn this buffer layer consists of pure Ge.

Table 1. Geometries of the Ge_{1-x} Sn_x grating antennas

	G1	G2	G3
Periodicity / μm	2.78	3.15	3.48
Width / μm	1.8	2.0	2.22

The doping concentration was validated using low temperature Hall effect measurements. For high doping concentrations the effect of the doping atoms onto the lattice parameter needs to be taken into account when calculating the Sn concentration [18]. Therefore, the measured doping concentration in combination with high resolution x-ray diffraction (XRD) measurements was used to calculate the Sn content. The Hall effect measurements were performed in a temperature range from 10 K to 300 K using Van-der-Pauw structures. The reflectivity and transmissivity data were obtained in a wavenumber range of 500 cm^{-1} to 7500 cm^{-1} using a Bruker Vertex 80 FTIR spectrometer in combination with a Bruker Hyperion 2000 microscope. The aperture was set to 100 100 $μm^2$ and 250 scans per measurement were used. For the reflectivity measurements an Au mirror was used as a reference and the transmission spectra were calibrated using the empty beam path.

The permittivities of the Ge_xSn_{1-x} layers were extracted from the reflectivity spectra obtained via FTIR measurements using the software RefFIT [19]. For the simulations of the extinction spectra of the comb-like antennas, a commercial finite difference time domain solver (Lumerical [20]) was used.

Optical Materials EXPRESS

3. Structural and electrical characterization results

Fig. 2 shows the XRD data obtained via 2 Theta/omega scans for all samples before and after PLM treatment. The high and narrow peak visible at about 69.2° originates from the (004) reflex of the Si-substrate. In all samples the small peak at 66.2° can be attributed to the Ge-VS. For the sample without Sn we see a double peak at 66° resulting from the p- and n-doped $Ge_{1-x}Sn_x$ layers. The separation is induced by the high Sb doping and the resulting shift of the peak. These peaks shift to smaller angles with increasing Sn concentration. This is a consequence of the increase in lattice constant of $Ge_{1-x}Sn_x$ with increasing Sn content, resulting in an increasing lattice mismatch with the Ge-VS. For the samples with a Sn concentration above 0%, the graded buffer forms an asymmetric peak at 65.9° due to the slow increase of the Sn concentration. A broadening of the peaks induced by the PLM treatment is visible. The samples were annealed at two energy densities, 0.3 Jcm^{-2} and 0.5 J/cm^2. The top layer melts during the PLM process. The thickness of the molten layer depends on the energy density and increases almost linearly with energy density. Here, the PLM at 0.3 J/cm^2 melts about 100 nm of GeSn alloy while annealing at 0.5 J/cm^2 melts slightly above 200 nm [21]. Next, within tens of microseconds the molten layer solidifies via liquid phase epitaxy. During the liquid phase the Sn and Sb is homogeneously redistributed over the entire molten layer and trapped at lattice position during so-called explosive epitaxy where the liquid/solid interface moves towards the surface with a velocity of 1-10 m/s. Such a fast and non-equilibrium recrystallization process decreases the concentration of interstitials and reduces the number of vacancies.

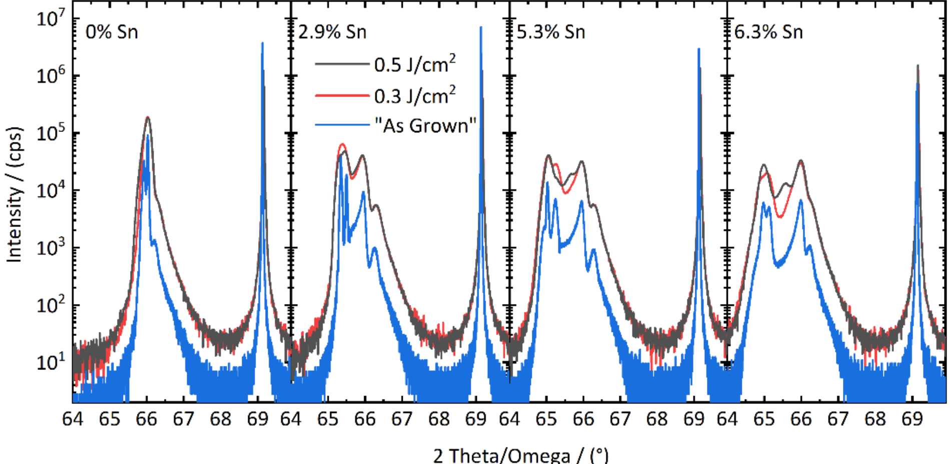

Fig. 2. 2 Theta/omega scans of the (004) reflection for all samples before and after PLM treatment measured with a Cu anode.

The in-plane and out-of-plane lattice parameters of the $Ge_{1-x}Sn_x$ layers were obtained from the reciprocal space maps (Fig. 3) and used to calculate the relaxed lattice parameter a_0 [22]. For the determination of the Sn concentration based on the lattice parameter a_0, the shift Δa_0 due to the incorporation of Sb into the $Ge_{1-x}Sn_x$ matrix needs to be taken into account. Therefore, the actual Sn concentration was calculated by iteratively correcting a_0 as follows:

$$\frac{\Delta a_0}{a_0} = \left(1 - \frac{r_{dopant}}{r_{GeSn}}\right) \frac{N_{dopant}}{N_{GeSn}}, \tag{1}$$

where the covalent radii r_{dopant} (r_{GeSn}) of Sb ($Ge_{1-x}Sn_x$), the dopant concentration N_{dopant} in cm^{-1} and the number N_{GeSn} of $Ge_{1-x}Sn_x$ atoms per cm^3 have been introduced. Since r_{GeSn}

Optical Materials EXPRESS

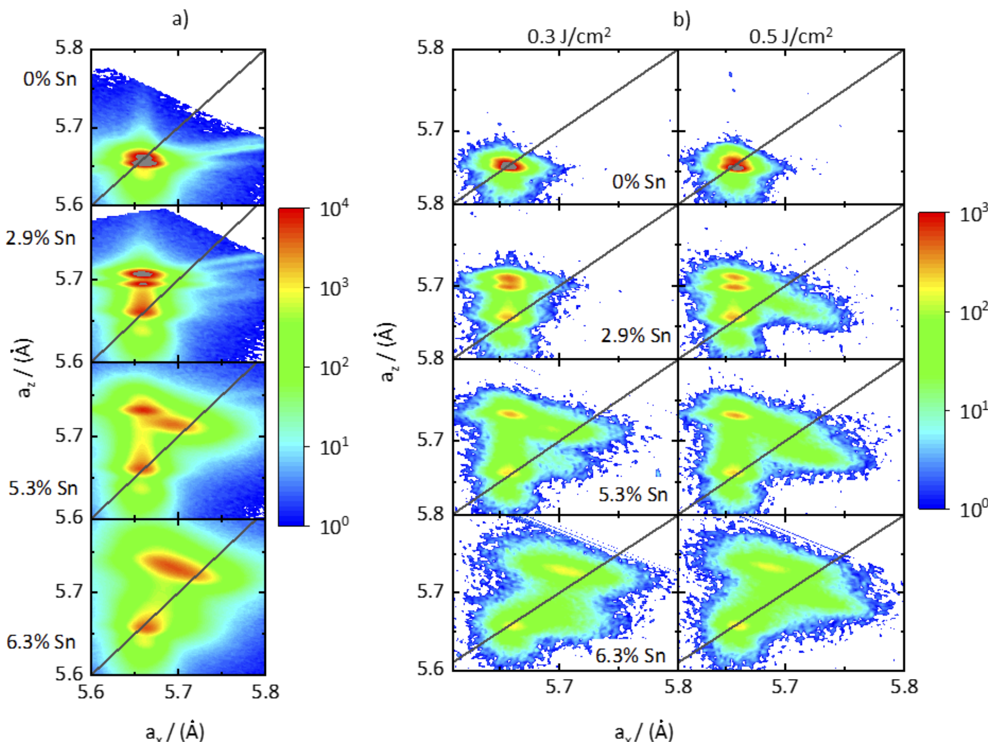

Fig. 3. Reciprocal space maps (converted to lattice parameter) showing the asymmetric $\bar{2}\bar{2}4$ reflections of the $Ge_{1-x}Sn_x$ peaks as well as the Ge-VS and the graded buffer and the relaxation lines before (a) and after (b) the PLM treatment. For the PLM samples, the left column shows PLM treatment with an energy density of 0.3 J/cm^2 and the right column with an energy density of 0.5 J/cm^2.

depends on the Sn concentration, it needs to be adjusted in each iteration [18,23]. Residual in-plane strain $\varepsilon_{\|}$ in the as-grown samples is low ($-0.0048 \leq \varepsilon_{\|} \leq 0.0006$).

While the nominal doping concentration $N_D = 310^{20}$ cm^{-3} is the same for all samples, the as-grown samples only show a fraction of the nominal doping as active doping concentration. The Hall effect measurements show that the active doping concentration can be drastically increased by the PLM treatment and the fraction of electrically active donors increases with increasing PLM energy density (Table 2). Typically, with increasing carrier concentration we expect the degradation of the carrier mobility due to the Coulomb scattering. But here for some combinations of PLM energy density and Sn concentration, the mobility even shows a slight increase that is direct proof of the significant improvement of the crystal quality due to lower concentration of scattering centres such as interstitial atoms and vacancies. According to the data presented in Table 2 the mobility improves for samples annealed with high energy density. This is because for the higher PLM energy density a larger fraction of the GeSn layer melts and recrystallizes via explosive liquid phase epitaxy compared to the GeSn layer in the samples annealed with 0.3 J/cm^2, where a lot of the initial defects from growth remain in the sample. The converted RSM data of the samples after the PLM treatment are shown in Fig. 3. In comparison to the as-grown samples one can see the onset of relaxation for a part of the 400 nm n^{++} layer. Together with the observation that while the active dopant concentration strongly increases the mobility also increases or stays the same (Table 2), this supports the assumption of an increase in crystal quality.

Optical Materials EXPRESS

Table 2. Compositional information obtained from XRD analysis and carrier concentrations as well as mobilities obtained from Hall effect measurements

Sample		PLM energy density J/cm^2	T = 10 K		T = 300 K		Sn XRD %	a_0 Å
			N_D (Hall) cm^{-3}	μ (Hall) cm^2/Vs	N_D (Hall) cm^{-3}	μ (Hall) cm^2/Vs		
	0	0	$4.18 \cdot 10^{19}$	153.3	$1.68 \cdot 10^{20}$	83.9		5.66
A.	1	0.3	$9.81 \cdot 10^{19}$	112.6	$2.43 \cdot 10^{20}$	39.5	0.3	-
	2	0.5	$1.35 \cdot 10^{20}$	298.6	$2.52 \cdot 10^{20}$	113.5		-
	0	0	$1.04 \cdot 10^{20}$	129.3	$1.72 \cdot 10^{20}$	52.8		5.68
B.	1	0.3	$2.32 \cdot 10^{20}$	108	$2.86 \cdot 10^{20}$	68.4	2.9	-
	2	0.5	$3.20 \cdot 10^{20}$	128	$3.23 \cdot 10^{20}$	85.7		-
	0	0	$1.07 \cdot 10^{20}$	95.1	$1.31 \cdot 10^{20}$	41.6		5.70
C.	1	0.3	$1.81 \cdot 10^{20}$	94.9	$2.25 \cdot 10^{20}$	64.1	5.3	-
	2	0.5	$2.08 \cdot 10^{20}$	102	$2.48 \cdot 10^{20}$	71.8		-
	0	0	$1.39 \cdot 10^{20}$	80.7	$2.47 \cdot 10^{20}$	35.9		5.71
D.	1	0.3	$3.41 \cdot 10^{20}$	65.7	$3.54\ 10^{20}$	49.6	6.3	-
	2	0.5	$4.03 \cdot 10^{20}$	74.3	$4.44 \cdot 10^{20}$	49.7		-

4. Optical characterization

To obtain the Drude parameters of the highly n-type doped layer we investigated the infrared reflectivity of the layers [24,25]. Fig. 4 shows the FTIR measurements of the reflectivity. All spectra were normalized to the reflectivity of an Au mirror.

With the assumption that the permittivity of the $Ge_{1-x}Sn_x$ layer can be described via a Drude term of the form

$$\varepsilon = \varepsilon_\infty - \frac{\omega_p^2}{\omega^2 + i\gamma\omega}, \tag{2}$$

we obtained the permittivity data from the reflectivity measurements using RefFIT [19]. In order to fit the data we used a three layer model consisting of the Si substrate with a variable permittivity of $9 \leqslant \varepsilon_1 \leqslant 20$ (setting $\varepsilon_2 = 0.1$) to take doping variations inside the substrate into account and a fixed thickness, followed by two layers with variable thicknesses. The first layer with a variable permittivity of $9 \leqslant \varepsilon_1 \leqslant 20$ (setting $\varepsilon_2 = 0.1$) represented the combined Ge-VS and the graded buffer. The topmost layer contained the Ge_xSn_{1-x} layer whose permittivity was modelled via a Drude term (Eq. (2)). The variable thickness was introduced to take local variations during the MBE growth into account as well as the uncertainty of the exact penetration depth of the PLM.

In order to be able to use the material permittivities for the simulation of the grating antennas our previous investigations have shown [11] that it is particularly important to accurately model the optical material properties at the resonance wavelength of the antennas, i.e. at wavelengths above 10 µm. Therefore, the fits need to be most accurate in the wavelength range between the plasma wavelength and the resonance wavelength. To ensure the best possible fit, we introduced a wavelength range with a weight factor of 10 for the region around the plasma frequency. The wavelength range is marked in each graph. Fig. 4 shows that we can fit the measured reflectivity with a large degree of accuracy and Table 3 shows the Drude parameter obtained from the fit. We see that we can decrease the plasma wavelength via the incorporation of Sn into the Ge crystal, achieving the lowest plasma wavelength of 3.6 µm for a Sn concentration of 2.9% of Sn. This is the lowest value obtained for any $Ge_{1-x}Sn_x$ alloy so far. In addition, we see that the plasma wavelength only slightly increases with more Sn incorporation in contrast to former investigations [11], potentially enabling these materials to be used in plasmonic applications.

Optical Materials EXPRESS

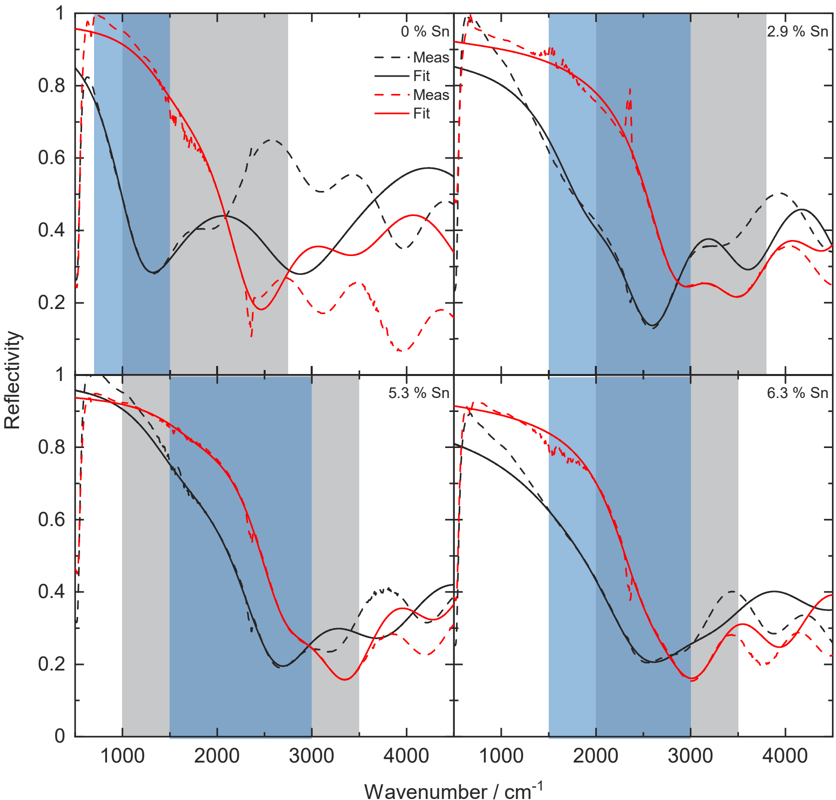

Fig. 4. Reflectivity spectra (dashed lines) and fitting functions (solid lines) for all samples after the PLM treatment. Black Spectra with a PLM energy density of 0.3 J/cm^2 and red spectra with 0.5 J/cm^2. Data obtained in the spectral range marked, as dark blue or grey was included in the fitting.

Table 3. Plasma wavelengths, relaxation times and ε_{inf} obtained for all samples based on optical measurements

Sn / %	PLM energy density/ J/cm^2	λ_p/µm	τ/fs	ε_{inf}	Sample Number
0	0.3	8.9	29	25	A.1
	0.5	4.6	41	24.5	A.2
2.9	0.3	5.0	8.2	20.1	B.1
	0.5	3.6	8.7	26.5	B.2
5.3	0.3	4.4	53	21.8	C.1
	0.5	3.8	15	25.3	C.2
6.3	0.3	4.7	5	19.1	D.1
	0.5	3.9	10	22	D.2

5. Plasmonic mode characterization and discussion

Figure 5 shows the extinction spectra of the comb-like antennas with three different geometries for all samples except for sample A.1, for which no extinction peak could be found. This can be ascribed to the high plasma wavelength of sample A.1. The extinction was calculated based on

Optical Materials EXPRESS

Table 4. Peak positions of the extinction peaks for all samples and geometries

Sn %	PLM energy density J/cm^2	λ_{peak} / µm		
		G1	G2	G3
0	0.3	-	-	-
	0.5	12.5	13.3	14.5
2.9	0.3	12.9	13.6	14.8
	0.5	11.6	12.9	13.9
5.3	0.3	12.1	13.8	14.9
	0.5	11.9	12.9	14.1
6.3	0.3	12.2	13.5	14.4
	0.5	12.6	13.8	14.5

the transmission obtained from the grating antennas T_{An} and the substrate background T_{BG}.

$$E = 1 - \frac{T_{An}}{T_{BG}}. \tag{3}$$

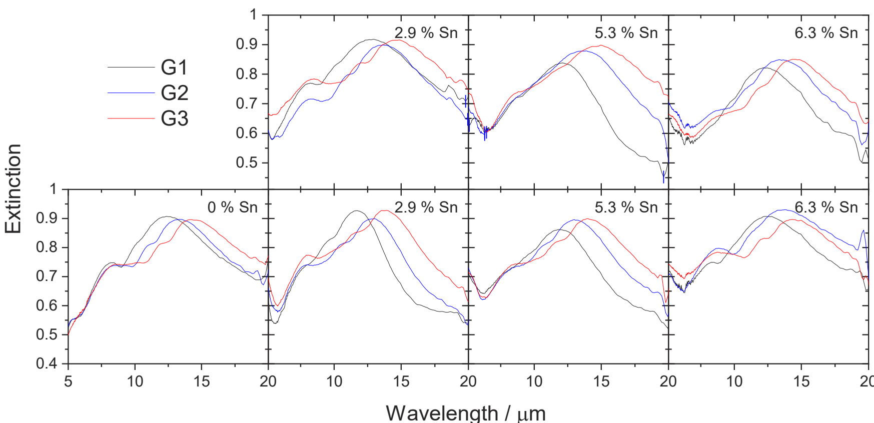

Fig. 5. Extinction spectra for all antenna geometries. Upper row with an energy density of 0.3 J/cm^2 lower row with an energy density of 0.5 J/cm^2.

All other samples show one distinct main peak, which shifts to higher wavelengths with higher width and higher pitch of the antennas (Table 4). This behaviour suggests that this extinction peak is due to a plasmonic mode, which forms at the interface of the comb-like antennas and the underlying layer, as we will discuss in more detail in the following. In contrast to former investigations [11], where identical antenna geometries fabricated from $Ge_{1-x}Sn_x$ layers grown directly on Si and without any post-growth treatment were investigated, we see that the peak extinction values do not decrease significantly with increasing Sn concentration even for a Sn concentration up to 6.3%. Figure 6 shows a comparison of the extinction spectra for geometry G1 for the Samples A.2 – D.2. We can see that for lower Sn concentrations of 2.9% or 5.3% the peaks are narrower and shifted to lower wavelengths compared to the peak obtained in the Ge sample. This shows that the optical properties of the grating antennas can be improved by the incorporation of Sn, demonstrating the potential of Sn rich Ge_xSn_{1-x} layers for plasmonic applications. For the sample containing 6.3% of Sn the peak shape is comparable to that of pure Ge, which we attribute to a decrease in crystal quality of the layer compared to samples with

Optical Materials EXPRESS

lower Sn content despite the Ge-VS and the graded buffer as a result of the increasing lattice mismatch of $Ge_{1-x}Sn_x$.and Ge with increasing Sn content. Besides the main extinction peak at around 10 µm the extinction spectra also show peaks at around 8 µm. We attribute these peaks to a plasmonic mode forming at the interface of the comb-like antennas and air. The measurements also show a weak shoulder between the two plasmonic peaks.

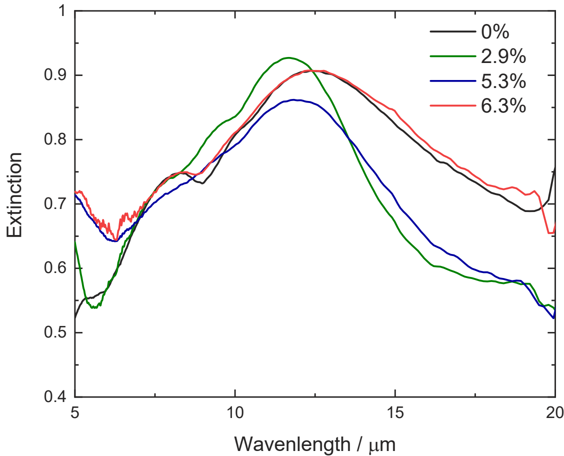

Fig. 6. Comparison of the geometry G1 for the samples A.2 –D.2.

Simulations were used to verify the plasmonic origin of the main peaks and to investigate the origin of the weak shoulder. For this simulation, the Si substrate as well as the Ge layer were assumed to be optical dielectric materials in the investigated MIR wavelength range. The refractive index of the Si substrate was set to 3.5 and the refractive index of the Ge layer was set to 4. The $Ge_{1-x}Sn_x$ layer was modelled with a wavelength dependent complex permittivity using the Drude parameters extracted from FTIR measurements. The polarization of the incident light was set to be parallel to the short axes of the antennas at a normal incidence angle. Since the PLM treatment does not stop precisely at the interface of the highly doped n- $Ge_{1-x}Sn_x$ layer and the p- Ge_xSn_{1-x} but somewhere inside the highly doped layer, it is not possible to assign the extracted Drude parameters to the whole volume of the antenna. To nonetheless investigate the optical behaviour of the antennas we simulated three different scenarios. First, we assumed that the whole antenna consists of material modelled by the extracted Drude parameters of the PLM layer. In a second approach the antenna was modelled to be composed of two layers, where the upper layer consisted of $Ge_{1-x}Sn_x$ modelled using the extracted PLM Drude parameters and the lower party consisted of $Ge_{1-x}Sn_x$ modelled using the extracted Drude parameters for the as-grown layer. In a third approach we assumed the antenna to fully consist of the as-grown material. Figure 7 shows the measurement results as well as simulation results for the geometry G2 of Sample B.1. In the targeted mid-IR region, the Si substrate as well as the Ge-VS can be modelled as materials with wavelength-independent refractive indices of $n_{\mathrm{Si}} = 3.5$ and $n_{\mathrm{Ge}} = 4$, respectively.

Depending on the Sn concentration and the PLM energy density, the thickness of the molten layers varies and therefore we can expect the measurements to be more accurately modelled with one of the three simulation models. In Fig. 7 it can clearly be observed that the multilayer approach shows the best agreement with measurements concerning both the peak positions as well as the peak heights. This strengthens the assumption that the PLM only has an effect on the highly doped $Ge_{1-x}Sn_x$ layer and does not affect the interface of the n- and p-type doped layers. By plotting the electrical field distribution for light of different wavelengths impinging

Optical Materials EXPRESS

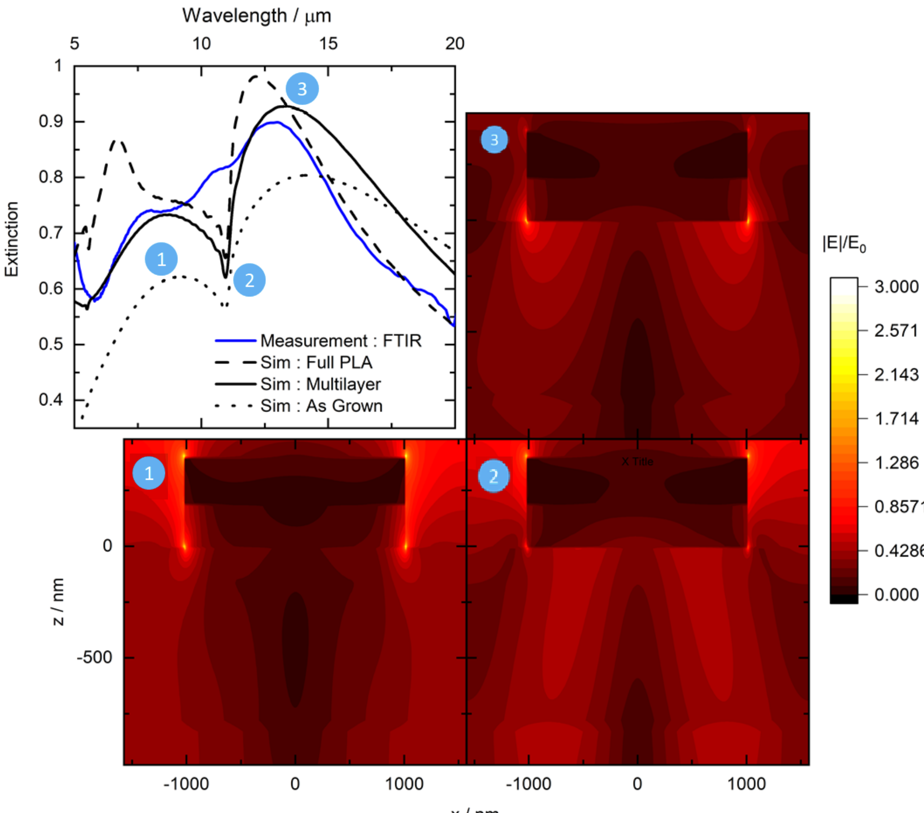

Fig. 7. Simulated and measured extinction spectra for different simulation approaches as well as cross-sectional plots of the amplitude of the electrical fields normalized to the amplitude of the incoming electrical field obtained from simulation for the multi-layer approach applied to sample B.1 and the geometry G2 at wavelengths corresponding to the peaks and dips shown in the extinction spectrum. The FDTD simulations were carried out using a gaussian light source with a normal angle of incidence and a polarization perpendicular to the comb like antennas.

onto the antenna, we can assign the measured extinction peaks to different plasmonic modes. At a wavelength of 8 µm (1) we observe that the extinction peak correlates with a strong electrical field mostly forming at the antenna-air interface showing that this extinction peak is due to the plasmonic air mode. For the peak (3) at 12.8 µm, we see the same behaviour but at the antenna-substrate interface, correlating the extinction peak to the plasmonic substrate mode. In addition to the strong electrical field enhancement of the plasmonic substrate mode we see that the electrical fields extend deeply into the substrate. This can be attributed to the formation of a Rayleigh anomaly (RA). The onset of the first order RA (11.025 µm) can be calculated via

$$\lambda_{RA} = \frac{P \cdot n_{Sub}}{m} \tag{4}$$

where P is the periodicity of the grating, n_{sub} =3.5 is the refractive index of the substrate and m = 1 is an integer. It was shown previously that the coupling of a plasmonic mode with a diffraction mode can lead to an asymmetric peak shape and very narrow extinction peaks [26], which we can clearly see in simulation. However, as the peak is slightly asymmetric, the sharp dip limiting the peak to lower wavelengths, which is clearly visible in the simulation, cannot be obtained in

Optical Materials EXPRESS

experiment. Indeed, at a wavelength of 11.25 µm, where simulations show a pronounced dip, the measured spectra exhibit a small peak instead. Investigating the electrical field distribution at 11.25 µm we see evidence of a RA penetrating into the substrate as expected as well as a strong field enhancement at the upper corners of the antenna correlated to a plasmonic air mode and only a weak field enhancement on the lower corners of the antennas correlated to the plasmonic substrate mode. Such an interaction of a plasmonic mode on the top of the grating antennas and a RA on the bottom could lead to a sharp increase in transmission, [27] which would lead to a dip in the extinction spectra. Since we obtain a peak rather than a dip in the measured spectra, we have to assume that none of these couplings occurs in our measured antennas. This could be due to several reasons such as fabrication imperfections due to the etching and lithography steps as well as sidewall roughness of the antennas or the unknown properties of the interface between the as-grown material and the molten material. Even if we cannot observe this narrowing of the plasmonic mode induced by coupling with other diffraction modes the plasmonic modes themselves are unaffected and we can see them clearly forming on the top and bottom party of the antennas.

6. Conclusion

We show an increase of the active doping concentration as well as the crystal quality of heavily doped $Ge_{1-x}Sn_x$ alloys by PLM treatment, enabling a plasma wavelength down to 3.6 µm for a Sn concentration of 2.9%. Due to the low plasma wavelength and the long relaxation time we were able to observe sharp plasmonic modes in grating antennas that could be excited at wavelengths below 10 µm, showing the potential of heavily doped $Ge_{1-x}Sn_x$ alloys for plasmonic applications. To further decrease the spectral width of the plasmonic modes, the coupling of the plasmonic mode with a diffractive mode (Rayleigh anomaly) needs to be optimized. In particular, the exact melting depth of the PLM treated layer as well as the structuring of the antennas has to be optimized to enable a strong coupling of both modes. Our results nonetheless show that the narrow plasmonic modes obtained in grating antennas fabricated from heavily doped $Ge_{1-x}Sn_x$ alloys are promising candidates for MIR plasmonic applications even at low wavelengths. Furthermore, we were able to show that there can be a net benefit in using highly doped $Ge_{1-x}Sn_x$ alloys instead of Ge for plasmonic applications if good crystal quality can be assured by choosing appropriate growth strategies and post-deposition treatments. In this context, a quantitative analysis in particular of the influence of the PLM treatment on the defect densities in GeSn alloys would be interesting. Furthermore, other doping strategies such as additional ex-situ doping [28] could be explored in order to further increase active dopant concentrations.

Funding. Bundesministerium für Bildung und Forschung (16ES1075).

Acknowledgment. This work was partially supported by the Bundesministerium für Bildung und Forschung (BMBF) under the project "ForMikro": Group IV heterostructures for high performance nanoelectronic devices (SiGeSn NanoFETs) (Project-ID: 16ES1075). We gratefully acknowledge provision of the Rigaku SmartLab XRD system by the group of Olav Hellwig at HZDR. In addition, we thank the 4th Physical Institute of the University of Stuttgart for the access to their FTIR Setup.

Disclosures. The authors declare no conflicts of interest.

Data availability. Data underlying the results presented in this paper are not publicly available at this time but may be obtained from the authors upon reasonable request.

References

1. M. L. Brongersma, N. J. Halas, and P. Nordlander, "Plasmon-induced hot carrier science and technology," Nat. Nanotechnol. **10**(1), 25–34 (2015).
2. E. Hardt, C. A. Chavarin, S. Gruessing, J. Flesch, O. Skibitzki, D. Spirito, G. M. Vita, G. de Simone, A. Di Masi, C. You, B. Witzigmann, J. Piehler, and G. Capellini, "Quantitative protein sensing with germanium THz-antennas manufactured using CMOS processes," Opt. Express **30**(22), 40265–40276 (2022).
3. M. I. Stockman, "Brief history of spaser from conception to the future," Adv. Photon. **2**(05), 2 (2020).

Optical Materials EXPRESS

4. J. A. Dionne, K. Diest, L. A. Sweatlock, and H. A. Atwater, "PlasMOStor: a metal-oxide-Si field effect plasmonic modulator," Nano Lett. **9**(2), 897–902 (2009).
5. L. Wang, Y. Zhang, and B. Wang, *et al.*, "High-performance infrared Ge-based plasmonic photodetector enhanced by dual absorption mechanism," APL Photonics **5**(9), 096104 (2020).
6. T. Taliercio and P. Biagioni, "Semiconductor infrared plasmonics," Nanophotonics **8**(6), 949–990 (2019).
7. J. Frigerio, A. Ballabio, and G. Isella, *et al.*, "Tunability of the dielectric function of heavily doped germanium thin films for mid-infrared plasmonics," Phys. Rev. B **94**(8), 085202 (2016).
8. R. Soref, J. Hendrickson, and J. W. Cleary, "Mid- to long-wavelength infrared plasmonic-photonics using heavily doped n-Ge/Ge and n-GeSn/GeSn heterostructures," Opt. Express **20**(4), 3814–3824 (2012).
9. C. Carraro, R. Milazzo, F. Sgarbossa, D. Fontana, G. Maggioni, W. Raniero, D. Scarpa, L. Baldassarre, M. Ortolani, A. Andrighetto, D. R. Napoli, D. de Salvador, and E. Napolitani, "N-type heavy doping with ultralow resistivity in Ge by Sb deposition and pulsed laser melting," Appl. Surf. Sci. **509**, 145229 (2020).
10. L. Baldassarre, E. Sakat, J. Frigerio, A. Samarelli, K. Gallacher, E. Calandrini, G. Isella, D. J. Paul, M. Ortolani, and P. Biagioni, "Midinfrared plasmon-enhanced spectroscopy with germanium antennas on silicon substrates," Nano Lett. **15**(11), 7225–7231 (2015).
11. F. Berkmann, M. Ayasse, J. Schlipf, F. Mörz, D. Weißhaupt, M. Oehme, S. Prucnal, Y. Kawaguchi, D. Schwarz, I. A. Fischer, and J. Schulze, "Plasmonic gratings from highly doped Ge 1−y Sn y films on Si," J. Phys. D: Appl. Phys. **54**(44), 445109 (2021).
12. L. Augel, I. A. Fischer, F. Hornung, M. Dressel, A. Berrier, M. Oehme, and J. Schulze, "Ellipsometric characterization of doped Ge < sub0.95</subSn < sub0.05</sub films in the infrared range for plasmonic applications," Opt. Lett. **41**(18), 4398–4400 (2016).
13. K. Lu Low, Y. Yang, G. Han, W. Fan, and Y.-C. Yeo, "Electronic band structure and effective mass parameters of $Ge_{1-x}Sn_x$ alloys," J. Appl. Phys. (Melville, NY, U. S.) **112**(10), 103715 (2012).
14. E. Kasper, M. Bauer, and M. Oehme, "Quantitative secondary ion mass spectrometry analysis of SiO_2 desorption during in situ heat cleaning," Thin Solid Films **321**(1-2), 148–152 (1998).
15. D. Schwarz, H. S. Funk, M. Oehme, and J. Schulze, "Alloy stability of $Ge_{1-x}Sn_x$ with Sn concentrations up to 17% utilizing low-temperature molecular beam epitaxy," J. Electron. Mater. **49**(9), 5154–5160 (2020).
16. M. Oehme, K. Kostecki, K. Ye, S. Bechler, K. Ulbricht, M. Schmid, M. Kaschel, M. Gollhofer, R. Körner, W. Zhang, E. Kasper, and J. Schulze, "GeSn-on-Si normal incidence photodetectors with bandwidths more than 40 GHz," Opt. Express **22**(1), 839–846 (2014).
17. A. Sobhani, M. W. Knight, Y. Wang, B. Zheng, N. S. King, L. V. Brown, Z. Fang, P. Nordlander, and N. J. Halas, "Narrowband photodetection in the near-infrared with a plasmon-induced hot electron device," Nat. Commun. **4**(1), 1643 (2013).
18. C. Xu, C. L. Senaratne, J. Kouvetakis, and J. Menéndez, "Experimental doping dependence of the lattice parameter in n -type Ge: Identifying the correct theoretical framework by comparison with Si," Phys. Rev. B **93**(4), 041201 (2016).
19. A. B. Kuzmenko, "Kramers–Kronig constrained variational analysis of optical spectra," Rev. Sci. Instrum. **76**(8), 083108 (2005).
20. Lumerical Inc., "FDTD: 3D Electromagnetic Simulator," https://www.lumerical.com/products/.
21. O. Steuer, D. Schwarz, M. Oehme, J. Schulze, H. Mączko, R. Kudrawiec, I. A. Fischer, R. Heller, R. Hübner, M. M. Khan, Y. M. Georgiev, S. Zhou, M. Helm, and S. Prucnal, "Band-gap and strain engineering in GeSn alloys using post-growth pulsed laser melting," J. Phys.: Condens. Matter **35**(5), 055302 (2023).
22. R. Beeler, R. Roucka, A. V. G. Chizmeshya, J. Kouvetakis, and J. Menéndez, "Nonlinear structure-composition relationships in the Ge 1−y Sn y /Si(100) (y<0.15) system," Phys. Rev. B **84**(3), 035204 (2011).
23. D. Weißhaupt, H. S. Funk, M. Kern, M. M. Dettling, D. Schwarz, M. Oehme, C. Sürgers, J. van Slageren, I. A. Fischer, and J. Schulze, "Weak localization and weak antilocalization in doped Ge1-y Sn y layers with up to 8% Sn," J. Phys.: Condens. Matter **33**(8), 085703 (2021).
24. C. Xu, J. Kouvetakis, and J. Menéndez, "Doping dependence of the optical dielectric function in n-type germanium," J. Appl. Phys. **125**(8), 085704 (2019).
25. J. Frigerio, A. Ballabio, K. Gallacher, V. Giliberti, L. Baldassarre, R. Millar, R. Milazzo, L. Maiolo, A. Minotti, F. Bottegoni, P. Biagioni, D. Paul, M. Ortolani, A. Pecora, E. Napolitani, and G. Isella, "Optical properties of highly n-doped germanium obtained by in situ doping and laser annealing," J. Phys. D: Appl. Phys. **50**(46), 465103 (2017).
26. E. M. Hicks, S. Zou, G. C. Schatz, K. G. Spears, R. P. van Duyne, L. Gunnarsson, T. Rindzevicius, B. Kasemo, and M. Käll, "Controlling plasmon line shapes through diffractive coupling in linear arrays of cylindrical nanoparticles fabricated by electron beam lithography," Nano Lett. **5**(6), 1065–1070 (2005).
27. J. M. McMahon, J. Henzie, T. W. Odom, G. C. Schatz, and S. K. Gray, "Tailoring the sensing capabilities of nanohole arrays in gold films with Rayleigh anomaly-surface plasmon polaritons," Opt. Express **15**(26), 18119–18129 (2007).
28. S. Prucnal, Y. Berencén, M. Wang, L. Rebohle, R. Böttger, I. A. Fischer, L. Augel, M. Oehme, J. Schulze, M. Voelskow, M. Helm, W. Skorupa, and S. Zhou, "Ex situ n+ doping of GeSn alloys via non-equilibrium processing," Semicond. Sci. Technol. **33**(6), 065008 (2018).